European Journal of Mechanics / A Solids 101 (2023) 105062

Contents lists available at ScienceDirect

European Journal of Mechanics / A Solids

journal homepage: www.elsevier.com/locate/ejmsol

Uni-axial stress–strain characterisation of silicone composite specimens derived from vocal folds replicas

Annemie Van Hirtum *, Mohammad Ahmad, Xavier Pelorson

LEGI, UMR CNRS 5519, Grenoble Alpes University, France

ARTICLE INFO

Keywords:
One-parameter non-linear elastic stress–strain model
Effective low-strain Young's modulus
Effective high-strain Young's modulus
Phenomenological model
Silicone composites
Mechanical vocal fold replica

ABSTRACT

A-priori knowledge of the uni-axial stress–strain behaviour of molded silicone multi-layer composite vocal folds replicas would benefit their structural design and favour their usage in physical studies of voiced speech sound production. Therefore, recently a model approach of the linear and continuous non-linear stress–strain behaviour of silicone composites is validated, for which the generic parameters are shown to depend only on the effective low-strain Young's modulus of the homogenised composite. Whereas previous work focused on extensive model validation in terms of layer's stacking and composition, in this work the model approach and uni-axial tension testing are used for the stress–strain characterisation of six molded silicone composite specimens derived from three vocal fold replicas. For each replica, measured and modelled effective low-strain Young's moduli are determined, the non-linear behaviour is assessed and a criterion is proposed to identify the onset strain and effective Young's modulus associated with a linear high-strain region and thus to extend the model approach to the high-strain region. It is concluded that the non-linear stress–strain behaviour of composite specimens can be predicted, solely based on the knowledge – either measured or modelled – of the effective low-strain Young's modulus of the equivalent homogenised composites. Consequently, uni-axial stress–strain behaviour can be taken into account for the structural design of silicone composites and associated multi-layer silicone vocal fold replicas.

1. Introduction

Human voiced speech sound production results from the vocal folds (VFs) auto-oscillation following a fluid–structure interaction at the glottis between airflow coming from the lungs and deformable VFs tissues (Rosen and Simpson, 2008; O'Shaughnessy, 1987). The positioning of the left and right VF on either side of the glottis is illustrated in Fig. 1(a). Despite the small VFs dimensions of only a few centimeters at most (O'Shaughnessy, 1987; Riede and Brown, 2013; Mobashir et al., 2018), the anatomical structure of a normal human VF is complex (Rosen and Simpson, 2008). It is often represented as consisting of superimposed layers (Rosen and Simpson, 2008). This VF representation, schematically depicted in Fig. 1(b), motivates deformable multi-layer (ML) silicone molded vocal fold replicas aiming to maintain, up to some degree, the anatomical multi-layer representation of a human VF, which consists of overlapping muscle (Mu), vocal ligament (Li), superficial (Su) and cover epithelium (Ep) layers. The elasticity of each molded silicone layer matches the order of magnitude observed for the corresponding layer in human passive soft VF tissues (as e.g. detailed in Table 2 of Section 2.1). Nevertheless, as the layers elasticity varies between replicas, the overall stress–strain behaviour of molded silicone replicas is likely to vary. So far however, their stress–strain behaviour is not *a-priori* known, instead it needs to be measured once replicas are molded. As the molding process is tedious and the resulting overall elasticity unknown, this limits the usage of silicone molded ML replicas in physical studies of the VFs auto-oscillation. This is particularly regrettable considering their potential for representing the multi-layer vocal folds structure. A-priori characterisation of the stress–strain behaviour of multi-layer silicone replicas would contribute to overcome this limitation and thus favour systematic physical studies of the impact of the VFs structure, in terms of layer properties, on their auto-oscillation in order to account for the variation of the VF's elasticity due to *e.g.* intra- and inter-speaker diversity (voice type, morphology, aging, breathing *etc.* Riede and Brown, 2013) or structural abnormalities (scar, nodule, carcinoma, cyst *etc.* Rosen and Simpson, 2008).

Steady vocal folds auto-oscillation is generally associated with small deformations and thus linear elasticity. Nevertheless, large deformations associated with non-linear elasticity can occur during abnormal auto-oscillation or during vocal folds adduction or abduction prior or following auto-oscillation. To encourage the structural design of multi-layer silicone replicas, an analytical elastic model approach of the

* Corresponding author.
E-mail address: annemie.vanhirtum@univ-grenoble-alpes.fr (A. Van Hirtum).

https://doi.org/10.1016/j.euromechsol.2023.105062
Received 11 February 2023; Received in revised form 14 June 2023; Accepted 18 June 2023
Available online 21 June 2023

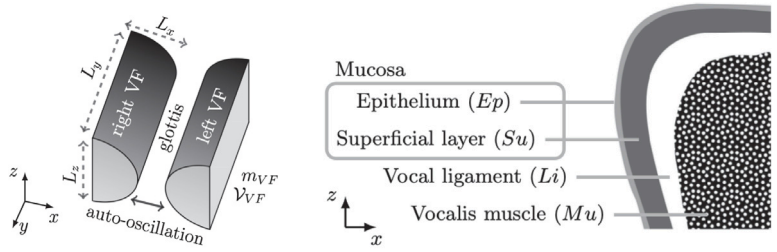

(a) left and right VF (b) multi-layer VF representation

Fig. 1. Schematic overviews: (a) right and left VFs positioning and overall properties — dimensions L_x, L_y, L_z, mass m_{VF} and volume $\mathcal{V}_{VF}$, auto-oscillation along the x-direction (b) multi-layer representation of the anatomical structure for a left VF.

low-strain linear (strains up to ≈0.3 Ahmad et al., 2021, 2022) and continuous non-linear (strains up to 1.55 Ahmad et al., 2023) stress–strain behaviour of silicone multi-layer composites was recently proposed. Models are obtained by considering equivalent homogenised composites as a function of their layers properties (dimensions, low-strain Young's modulus $\mathcal{E}$ and stacking orientation). The model approach was extensively validated from uni-axial tension tests on multi-layer silicone bone-shaped specimens with up to seven layers in the test section (Fig. 2(b)). As for single layer specimens, the observed deformation for composite specimens was elastic and no plastic deformation was observed following unloading. Molded silicone composites in Ahmad et al. (2021, 2022, 2023) were designed in order to assure model validation and not to represent the composition of multi-layer silicone replicas. The aim of this work is thus to study the stress–strain behaviour of multi-layer silicone composite specimens derived from three commonly used silicone ML vocal folds replicas using uni-axial tension tests and the analytical model approach. In case that the model approach allows an *a-priori* measurement-free estimation of the stress–strain behaviour, it can be applied to composites representing other silicone VF replicas so that their stress–strain behaviour can be compared. The current study aims thus not just at evidence based modelling and characterisation of the stress–strain behaviour of replica-based specimens, but is also a first necessary step towards the *a-priori* structural design of multi-layer silicone VF replicas in terms of their stress–strain behaviour. Eventually, this contributes to the development of systematic physical studies of the auto-oscillation of deformable multi-layer silicone VFs replicas with normal or abnormal VFs structure. In the long term the prospect of systematic studies might contribute to predict the effect of the VF structure on auto-oscillation features related to voice quality and on the planning of clinical interventions on the VFs structure.

Three molded ML silicone VFs replicas (M5, MRI and EPI) are detailed in Section 2.1. In Section 2.2, six ML composite silicone bone-shaped specimens are derived from these three vocal folds replicas. Experimental stress–strain data, appropriate models and their parameter fitting is outlined in Section 3. The prediction of model parameters is then outlined in Section 4. Measured and predicted parameter values and the associated stress–strain curves are discussed in Section 5. The conclusion is formulated in Section 6.

2. From three ML silicone replicas to six ML silicone specimens

2.1. Three ML silicone replicas: M5, MRI and EPI

Deformable multi-layer (ML) silicone vocal folds replicas aim to mimic, up to some degree, the anatomical multi-layer representation (Ep, Su, Li, Mu) of a human VF depicted in Fig. 1(b). In literature, two-layer (Su and Mu) (Scherer et al., 2001), three-layer (Ep, Su and Mu) (Tokuda and Shimamura, 2017; Pickup and Thomson, 2010) and four-layer (Ep, Su, Li and Mu) (Murray and Thomson, 2012) VF replicas are proposed. Concretely, replicas used in Tokuda and Shimamura (2017), Bouvet et al. (2020b, 2021) and Van Hirtum et al. (2022)

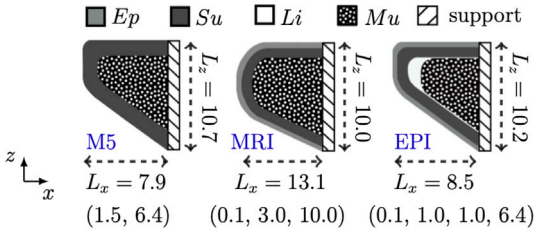

(a) silicone VF replicas: M5, MRI and EPI

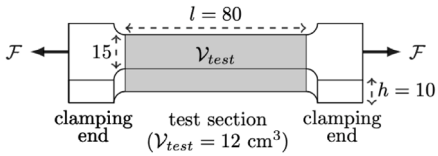

(b) bone-shaped specimen

Fig. 2. Schematic overviews: (a) multi-layer silicone VF replicas with dimensions (in mm) L_x, L_z: two-layer M5, three-layer MRI and four-layer EPI. Single layer dimensions along the x-direction l_x are indicated between round brackets (in mm). (b) Bone-shaped specimen with test section dimensions (in mm) and volume $\mathcal{V}_{test}$. The force $\mathcal{F}$ direction (arrows) for uni-axial stress testing is indicated.

Table 1
Overall properties for M5, MRI and EPI replicas and values reported for a male adult (Hirano et al., 1983; Plant et al., 2004; Mobashir et al., 2018; Alexander et al., 2021) and using soft tissue density 1.03 g/cm^3 (Riede and Brown, 2013; Titze, 2011): right–left length L_x, posterior-anterior length L_y, inferior–superior length L_z, volume $\mathcal{V}_{VF}$ and mass m_{VF}.

	L_x [mm]	L_y [mm]	L_z [mm]	$\mathcal{V}_{VF}$ [mm^3]	m_{VF} [g]
M5	7.9	17.0	10.7	1025	0.96
MRI	13.1	18.0	10.0	1707	1.57
EPI	8.5	17.0	10.2	1079	1.01
Human	7–8	15–25	4–8	610–830	0.61–0.82

– conventionally labelled M5 (two-layer), MRI (three-layer) and EPI (four-layer) – are schematically depicted in Fig. 2(a). Single layer dimensions l_x (in mm) along the main auto-oscillation direction, *i.e.* the x-direction, are given between round brackets. Overall replica properties shown in Fig. 1(a) are summarised in Table 1 indicating right–left length L_x, posterior–anterior length L_y, inferior–superior length L_z, total mass m_{VF} and volume $\mathcal{V}_{VF}$. As a reference, typical values reported for the VF of a male adult are given as well (Hirano et al., 1983; Plant et al., 2004; Mobashir et al., 2018; Alexander et al., 2021; Riede and Brown, 2013; Titze, 2011).

The low-strain elastic Young's modulus $\mathcal{E}$ of each layer of these VF replicas varies in the range up to 65 kPa in order to approximate elasticity values associated with human VFs layers, *i.e.* muscle layer 8–29 kPa, ligament layer 10–45 kPa, superficial layer 2–9 kPa and

Table 2
Single layer properties for M5, MRI and EPI replicas (Bouvet et al., 2020b; Bouvet, 2019; Ahmad et al., 2021): low-strain Young's modulus $\mathcal{E}$, normalised layer length l_x/L_x and normalised volume $\mathcal{V}/\mathcal{V}_{VF}$.

	$\mathcal{E}$ [kPa]				l_x/L_x [%]			$\mathcal{V}/\mathcal{V}_{VF}$ [%]		
	Human	M5	MRI	EPI	M5	MRI	EPI	M5	MRI	EPI
Muscle (Mu)	8–29	14.4	4.0	23.4	81.0	76.3	75.2	50.0	68.5	38.1
Ligament (Li)	10–45	–	–	4.0	–	–	11.8	–	–	7.6
Superficial (Su)	2–9	4.0	2.2	2.2	19.0	22.9	11.8	50.0	27.5	50.3
Epithelium (Ep)	40–60	–	64.7	64.7	–	0.8	1.2	–	4.0	4.0

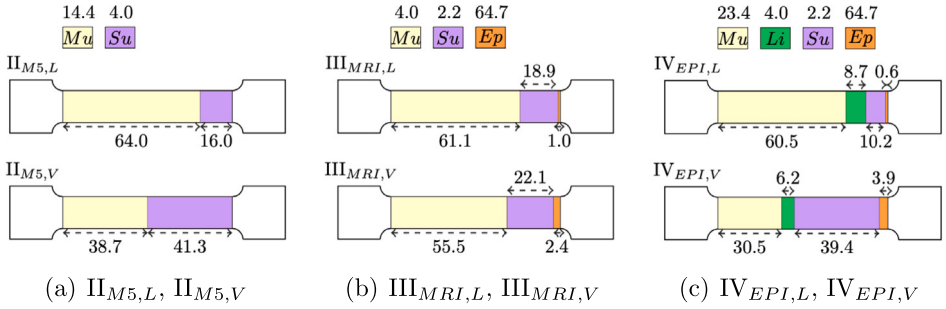

(a) II$_{M5,L}$, II$_{M5,V}$ (b) III$_{MRI,L}$, III$_{MRI,V}$ (c) IV$_{EPI,L}$, IV$_{EPI,V}$

Fig. 3. Molded length-based (subscript L) and volume-based (subscript V) bone-shaped silicone composites derived from the multi-layer M5, MRI and EPI silicone replicas (Fig. 2(a)): (a) two-layer ($n = 2$) II$_{M5,L}$ and II$_{M5,V}$, (b) three-layer ($n = 3$) III$_{MRI,L}$ and III$_{MRI,V}$, (c) four-layer ($n = 4$) IV$_{EPI,L}$ and IV$_{EPI,V}$. Legends specify layer's low-strain Young's modulus $\mathcal{E}_{i=1\ldots n}$ (in kPa) matching the corresponding Muscle-Mu, Ligament-Li, Superficial-Su or Epithelium-Ep layer in Table 2. Layer lengths $l_{i=1\ldots n}$ (in mm) are indicated.

epithelium layer 40–60 kPa (Hirano et al., 1983; Alipour and Titze, 1991; Berke and Gerratt, 1993; Min et al., 1995; Chan et al., 2007; Miri, 2014; Zhang et al., 2017; Chhetri et al., 2011). Concretely, all layers are molded from elastomer silicone mixtures at different mass mixing ratios, *i.e.* either Thinner-Ecoflex or Thinner-Dragonskin mixtures (Smooth-On Inc.). The relative mass portion of silicone Thinner is varied up to 8 whereas the relative mass portion of Ecoflex or Dragonskin is held constant to 2 in accordance with the molding procedure detailed in Pickup and Thomson (2010), Murray and Thomson (2012), Tokuda and Shimamura (2017), Bouvet (2019) and Bouvet et al. (2020b). The low-strain linear Young's modulus of each silicone mixture is obtained from uni-axial tension testing on bone-shaped specimens as the one schematically depicted in Fig. 2(b). In Ahmad et al. (2021, 2022), the reproducibility of these elastomer silicone mixtures and repeatability of uni-axial stress–strain measurements at room temperature (21 ± 2 °C) was extensively validated for two different uni-axial tension test methods, *i.e.* using a mechanical press (Instron 3369 series) and a developed precision loading setup. Elastic deformation was observed for all mixtures and no plastic deformation was observed following unloading. Resulting layer properties for the M5, MRI and EPI replicas (Fig. 2(a)) are summarised in Table 2 in terms of low-strain Young's modulus $\mathcal{E}$, normalised layer length l_x/L_x along the auto-oscillation direction and normalised volume $\mathcal{V}/\mathcal{V}_{VF}$ (Bouvet et al., 2020b; Bouvet, 2019; Ahmad et al., 2021). From Table 2 is seen that layer properties vary considerably between replicas. Considering the low-strain Young's modulus, it is seen that although the order of magnitude observed for passive vocal folds tissues is respected for all layers, the muscle and superficial layers increase and decrease with 60% and 81% respectively when comparing the M5 and EPI replicas.

2.2. Six replica-based bone-shaped ML silicone specimens

Six bone-shaped ML silicone specimens, depicted in Fig. 3, are molded based on the M5, MRI and EPI replicas shown in Fig. 2(a). Each specimen consists of a beam-shaped test section (length $l = 80$ mm, width 15 mm, thickness 10 mm and volume $\mathcal{V}_{test} = 12$ cm^3) in between two clamping ends as depicted in Fig. 2(b). Specimens with n layers ($n \in \{2, 3, 4\}$) are designed as two-layer (label II$_{M5}$ for M5-based, $n = 2$), three-layer (label III$_{MRI}$ for MRI-based, $n = 3$) or four-layer (label IV$_{EPI}$ for EPI-based, $n = 4$) composites so that each layer has the low-strain Young's modulus $\mathcal{E}$ as indicated in Table 2. All layers are stacked serially, *i.e.* perpendicular with respect to the force direction shown in Fig. 2(b). Consequently, each layer has constant width (15 mm) and constant height (10 mm). Layer lengths l_i, with layer index $i = 1 \ldots n$, are imposed either so that l_i/l matches normalised lengths l_x/L_x along the main auto-oscillation direction (length-based, subscript L) or so that $\mathcal{V}_i/\mathcal{V}_{test}$ matches normalised volumes $\mathcal{V}/\mathcal{V}_{VF}$ (volume-based, subscript V) as an overall replica property. Table 2 provides an overview of the corresponding l_x/L_x and $\mathcal{V}/\mathcal{V}_{VF}$ values for all replica layers (Mu, Li, Su or Ep). From Fig. 2(a) is seen that the two molded composites derived from each replica differ considerably in terms of layer lengths l_i (measured with a laser transceiver, Panasonic HL-G112-A-C5, wavelength 655 nm, accuracy 8 µm). Compared to length-based specimens (upper row in Fig. 3), volume-based specimens (lower row in Fig. 3) result in decreased lengths of the muscle (Mu) and ligament (Li) layer and increased lengths of the superficial (Su) and epithelium (Ep) layers. Molded composites are labelled II$_{M5,L}$ and II$_{M5,V}$ for the M5 replica, III$_{MRI,L}$ and III$_{MRI,V}$ for the MRI replica and IV$_{EPI,L}$ and IV$_{EPI,V}$ for the EPI replica. The overall molding accuracy of the layers yields ±0.72 mm, which is within the range previously reported (Ahmad et al., 2022).

3. Experimental stress–strain data characterisation

3.1. Stress–strain data from uni-axial tension testing

The stress–strain behaviour of the six molded silicone ML specimens is measured at room temperature (21±2 °C) from uni-axial tension tests by means of precision loading (Ahmad et al., 2021, 2022). Briefly, the force–elongation relationship $\mathcal{F}(\Delta l)$ along the force direction, indicated in Fig. 2(b), is measured on vertically placed specimens by fixing the upper clamping end and adding a known weight m (calibrated scale, Vastar 500G X 0.01G, accuracy 0.01 g) to the lower clamping end. The weight is incremented with 2.3 ± 1.9 g. The load force $\mathcal{F}$ for added mass m is $\mathcal{F} = m \cdot g_0$ with gravitational constant $g_0 = 9.81$ m/s^2. For each weight increment, the specimens elongation Δl is obtained as $\Delta l = \sum_{i=1}^{n} \Delta l_i$ with Δl_i the measured elongation of each layer (ruler, accuracy 0.05 mm). Depending on the specimen, the assessed total elongation varies between 44 mm and 198 mm, corresponding to a total added weight between 14.5 g and 125.8 g. Measured force–elongation data are illustrated in Fig. 4(a). As for specimens assessed in Ahmad et al. (2021, 2022) elastic deformation is observed for all specimens.

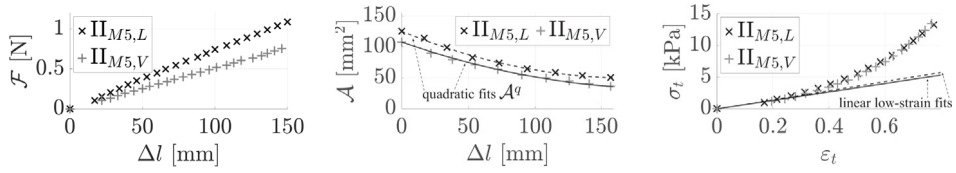

(a) $\mathcal{F}(\Delta l)$ (b) $\mathcal{A}(\Delta l)$ (c) $\sigma_t(\varepsilon_t)$

Fig. 4. Examples of uni-axial stress tests data for M5-based specimens $\mathrm{II}_{M5,L}$ (×) and $\mathrm{II}_{M5,V}$ (+): (a) force–elongation data $\mathcal{F}(\Delta l)$, (b) area–elongation data $\mathcal{A}(\Delta l)$ and quadratic fits $\mathcal{A}^q(\Delta l)$ with $R^2 = 99\%$ (lines) and (c) stress–strain curves $\sigma_t(\varepsilon_t)$ with best linear fits (lines) to the linear low-strain range $\varepsilon_t \leq 0.32$ with $R^2 > 96\%$ corresponding to measured low-strain effective Young's modulus $\mathcal{E}_{eff} = 8.0$ kPa for $\mathrm{II}_{M5,L}$ (dashed linear slope) and $\mathcal{E}_{eff} = 7.2$ kPa for $\mathrm{II}_{M5,V}$ (full linear slope).

The area–elongation relationship $\mathcal{A}(\Delta l)$ for each specimen is obtained from measuring the layers midway cross-sectional area perpendicular to the force $\mathcal{A}_i$ (caliper Vernier, accuracy 0.02 mm). The cross-sectional area $\mathcal{A}$ results from the weighted arithmetic mean as

$$\mathcal{A} = \frac{\sum_{i=1}^{n}(l_i + \Delta l_i)\mathcal{A}_i}{l + \Delta l}. \tag{1}$$

The specimens cross-section area $\mathcal{A}$ is measured whenever the elongation increment yields 12.6 ± 5.2 mm, corresponding to a weight increment of 6.0 ± 5.0 g. A quadratic fit (coefficient of determination $R^2 \geq 98\%$) is applied to the measured $\mathcal{A}(\Delta l)$ data for each specimen resulting in a continuous approximation $\mathcal{A}^q(\Delta l)$. Measured area–elongation data $\mathcal{A}(\Delta l)$ and fitted curves $\mathcal{A}^q(\Delta l)$ are illustrated in Fig. 4(b).

Experimental true stress–strain curves $\sigma_t(\varepsilon_t)$ are then obtained from the instantaneous force–elongation $\mathcal{F}(\Delta l)$ and area-elongation curves $\mathcal{A}^q(\Delta l)$ as

$$\sigma_t = \frac{\mathcal{F}}{\mathcal{A}^q}, \tag{2a}$$

$$\varepsilon_t = \ln\left(\frac{l + \Delta l}{l}\right). \tag{2b}$$

The total elongations measured correspond to the following strain ranges: $\varepsilon_t \leq 1.08$ for specimens $\mathrm{II}_{M5,L}$ and $\mathrm{II}_{M5,V}$, $\varepsilon_t \leq 0.49$ for specimens $\mathrm{III}_{MRI,L}$ and $\mathrm{III}_{MRI,V}$ and $\varepsilon_t \leq 0.44$ for specimens $\mathrm{IV}_{EPI,L}$ and $\mathrm{IV}_{EPI,V}$.

3.2. Experimental characterisation: best fit stress–strain model parameters

3.2.1. Linear model fitting: low-strain and high-strain Young's modulus

The effective low-strain elastic Young's modulus $\mathcal{E}_{eff}$ of each ML specimen is obtained experimentally as the slope of the linear best fits to the measured stress–strain data for strains up to upper low-strain limit ε_l, *i.e.* the elastic low-strain region $\varepsilon_t \leq \varepsilon_l$, in which the stress σ_t is proportional to the strain ε_t, so that

$$\mathcal{E}_{eff} = \frac{\sigma_t}{\varepsilon_t}, \tag{3}$$

expressing linear elastic stress–strain behaviour. The upper limit of the low-strain range for each specimen, summarised in Table 3, is obtained as the range for which linear fit accuracy R^2 is maximum (Ahmad et al., 2021, 2022) ($R^2 \geq 97\%$ holds). The mean and standard deviation of the overall upper limit of the linear low-strain region yields $\varepsilon_l = 0.28 \pm 0.03$ which corresponds to an elongation of 37 ± 7 mm. This value is consistent with $\varepsilon_l = 0.30 \pm 0.10$ reported in Ahmad et al. (2021) and $\varepsilon_l = 0.26 \pm 0.02$ in Ahmad et al. (2022). Examples of experimental stress–strain data $\sigma_t(\varepsilon_t)$ and associated linear fits ($R^2 > 99\%$) to the linear low-strain region $\varepsilon_t \leq \varepsilon_l$ are illustrated in Fig. 4(c).

Linear stress–strain behaviour can occur again at sufficiently large strains, such as observed for biological tissues (Fung, 1967, 2010; Tanaka et al., 2011), corresponding to the linear high-strain range $\varepsilon_t^{NL} \leq \varepsilon_t$, with ε_t^{NL} denoting the lower limit of the linear high-strain range and $\varepsilon_l \ll \varepsilon_t^{NL}$. The same way as outlined for the effective low-strain elastic Young's modulus $\mathcal{E}_{eff}$, the effective high-strain Young's modulus $\mathcal{E}_{NL}$ can be obtained as the slope of the linear best fits to stress–strain curves in the high strain range.

Table 3
Measured elastic low-strain upper limit ε_l.

L-based	ε_l	V-based	ε_l
$\mathrm{II}_{M5,L}$	0.31	$\mathrm{II}_{M5,V}$	0.32
$\mathrm{III}_{MRI,L}$	0.29	$\mathrm{III}_{MRI,V}$	0.25
$\mathrm{IV}_{EPI,L}$	0.25	$\mathrm{IV}_{EPI,V}$	0.26

3.2.2. Non-linear continuous models: best fit two-parameter sets

In Ahmad et al. (2023), measured stress–strain data $\sigma_t(\varepsilon_t)$ for silicone composites are approximated continuously for $\varepsilon_t \leq 1.55$, covering the linear low-strain and subsequent non-linear strain range, using the either an exponential (E) or cubic (C) continuous two-parameter relationship, which are shown to nearly match for strains up to 1.55 and are given as:

$$\text{exponential} - \text{E: } \sigma_t(\varepsilon_t) = A\,(e^{B\,\varepsilon_t} - 1), \tag{4a}$$

$$\text{cubic} - \text{C: } \sigma_t(\varepsilon_t) = a\,\varepsilon_t^3 + b\,\varepsilon_t, \tag{4b}$$

with (A, B) and (a, b) their respective two-parameter sets. The near match of both continuous relationships is further confirmed considering measured stress–strain data for the silicone specimens (Fig. 3) as the accuracy associated with the best fits obtained by minimising the root mean square error (rmse in kPa) between fitted and measured stress–strain data yields $R^2 \geq 99.9\%$ and rmse < 0.3 kPa. Best fits are illustrated in Fig. 5 for specimens $\mathrm{II}_{M5,L}$ and $\mathrm{II}_{M5,V}$ for the exponential (Fig. 5(a)) and cubic (Fig. 5(b)) relationship. In the following, curves obtained with the best fit parameter estimates (suffix -fit) are denoted E-fit and C-fit for the exponential and cubic relationship, respectively. Estimated best fit parameters are denoted $(\widehat{A}, \widehat{B})$ for the exponential and $(\widehat{a}, \widehat{b})$ for the cubic relationship, respectively.

4. Analytical stress–strain model parameter prediction

4.1. Linear low-strain range: predicted effective low-strain Young's modulus

In Section 3.2.1 is shown that Hooke's law of linear elastic deformation (Eq. (3)) holds in the low-strain range $\varepsilon_t \leq \varepsilon_l$. The linear low-strain stress–strain relationship is thus characterised by the elastic Young's modulus. As each specimen consists out of n serial stacked layers, Reuss's hypothesis (Reuss, 1929) of homogeneous stress can be applied. This implies that the stress σ_t in an equivalent homogeneous composite and the stress $\sigma_{t,i=1\ldots n}$ in each layer is assumed constant so that $\sigma_{t,i=1\ldots n} = \sigma_t$. The effective low-strain Young's modulus of the equivalent homogeneous composite with length $l = \sum_{i=1}^{n} l_i$ is then modelled as the harmonic mean of the layers Young's moduli $\mathcal{E}_i$ weighted with their lengths l_i as

$$\widehat{\mathcal{E}}_{eff} = \frac{\sum_{i=1}^{n} l_i}{\sum_{i=1}^{n}\left(\frac{l_i}{\mathcal{E}_i}\right)}. \tag{5}$$

This low-strain model of the effective Young's modulus was extensively validated (accuracy 2.4 kPa) for multi-layer silicone specimens (Ahmad et al., 2021, 2022).

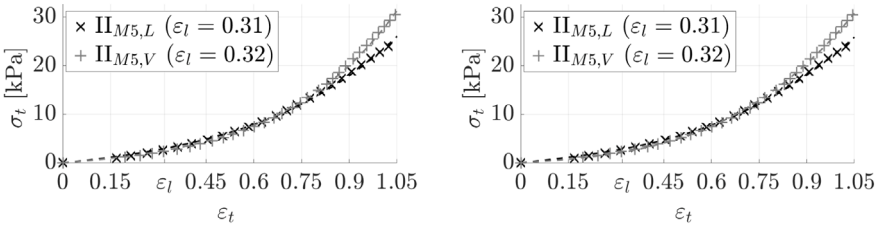

(a) best exponential fit (b) best cubic fit

Fig. 5. Examples of measured stress–strain data for specimens $\mathrm{II}_{M5,L}$ (×) and $\mathrm{II}_{M5,V}$ (+) and non-linear continuous best fits (dashed lines) with $R^2 \geq 99.9\%$ and rmse < 0.3 kPa using best fit parameters sets of two-parameter relationships: (a) exponential, (b) cubic. Linear low-strain limit ε_l is indicated.

4.2. Linear and non-linear stress–strain range: predicted two-parameter sets

Two-parameter exponential (E) and cubic (C) relationships expressed in Eq. (4) both hold (Section 3.2.2) for the assessed strain range comprising the linear low-strain range ($\varepsilon_t \leq \varepsilon_l$) and the non-linear strain range beyond ($\varepsilon_t > \varepsilon_l$). In Ahmad et al. (2023) two generic two-parameter sets were derived using the assumption that both relationships nearly match for strains in the interval $\varepsilon_t \leq 1.55$. The assumption is motivated from the experimental characterisation and from analytical reasoning in Ahmad et al. (2023) and confirmed for the measured stress–strain data on the six replica-based specimen in Section 3.2.2. Generic expressions allow to predict the two-parameter sets (A, B) for the exponential and (a, b) for the cubic relationships in the strain range $\varepsilon_t \leq 1.55$.

Firstly, generic two-parameter sets are obtained analytically from an analysis of the exponential and cubic relationships in Eq. (4). The resulting generic model-based parameter sets (suffix -M) depend on $\mathcal{E}_{eff}$ as

$$\text{modelled exponential } (A, B) \text{ – E-M: } (\mathcal{E}_{eff}/2.15,\ 2.15), \tag{6a}$$

$$\text{modelled cubic } (a, b) \text{ – C-M: } (2.53\,\mathcal{E}_{eff},\ \mathcal{E}_{eff}). \tag{6b}$$

It is noted that expressions for a and B satisfy the condition $a = \frac{1}{6}B^2\mathcal{E}_{(eff)}$. This condition, obtained from a third order Taylor series expansion of the exponential relationship (Eq. (4)), follows from the assumption of nearly matching exponential and cubic relationships (Ahmad et al., 2023).

Thus, from generic model-based parameter sets in Eq. (6) is seen that values are either constant (for B) or vary linearly with $\mathcal{E}_{eff}$ (for A, a and b). These dependencies are then exploited in Ahmad et al. (2023) to propose another pair of generic two-parameter sets by imposing either the linear (for A, a and b) or the constant (for B) relationship to the exponential and cubic best fit parameters estimated on the stress–strain data curves of 40 silicone composite specimens (with a low-strain Young's modulus up to 65 kPa). The resulting overall generic approximated parameter sets (suffix -A) are thus either constant or linearly proportional to $\mathcal{E}_{eff}$ and are given as:

$$\text{approximated exponential } (A, B) \text{ – E-A: } (\mathcal{E}_{eff}/3.03,\ 2.21), \tag{7a}$$

$$\text{approximated cubic } (a, b) \text{ – C-A: } (1.78\,\mathcal{E}_{eff},\ 0.92\,\mathcal{E}_{eff}). \tag{7b}$$

Both the generic model-based parameter sets (Eq. (6), suffix -M) and the generic approximated parameter set (Eq. (7), suffix -A) depend only on the effective low-strain Young's modulus $\mathcal{E}_{eff}$, which can be either modelled (Eq. (5)) or obtained experimentally as the slope of stress–strain data in the low-strain range $\varepsilon_t \leq \varepsilon_l$ (Section 3.2.1). Consequently, for both generic two-parameter sets, the non-linear model approach as a function of $\mathcal{E}_{eff}$ reduces to a one-parameter model approach. Furthermore, for the continuous cubic and exponential relationships low-strain, it is noted that linear stress–strain behaviour is obtained from a first order Taylor series expansion (Ahmad et al., 2023). The low-strain Young's modulus in terms of the continuous parameters is then obtained as the parameter product $A\,B$ and linear parameter b for the exponential and the cubic relationship respectively. Thus concretely, for the generic model-based parameter sets (Eq. (6)) this yields $b = \mathcal{E}_{eff}$ and $A\,B = \mathcal{E}_{eff}$ and for the generic approximated parameter sets (Eq. (7)) this becomes $b = 0.92\,\mathcal{E}_{eff}$ and $AB = 0.73\,\mathcal{E}_{eff}$.

4.3. Linear high-strain range: predicted effective high-strain Young's modulus

In Ahmad et al. (2023), the effective high-strain Young's modulus $\mathcal{E}_{NL}$ associated with a linear high-strain range $\varepsilon_t^{NL} \leq \varepsilon_t$ is predicted by considering the local slope of the continuous exponential and cubic stress–strain relationships (Eq. (4)). Local slopes are obtained from a first order expansion of the exponential and cubic relationships at ε_t^{NL} as:

$$\text{exponential high-strain } \mathcal{E}_{NL}\text{: } \mathcal{E}_{NL}/\mathcal{E}_{eff} = e^{B\,\varepsilon_t^{NL}}, \tag{8a}$$

$$\text{cubic high-strain } \mathcal{E}_{NL}\text{: } \mathcal{E}_{NL}/\mathcal{E}_{eff} = 3\,k\,(\varepsilon_t^{NL})^2 + 1, \tag{8b}$$

with $k = a/\mathcal{E}_{eff}$ in Eq. (8b). It is found for both the exponential and cubic stress–strain relationships that $\mathcal{E}_{NL}$ is linearly proportional to $\mathcal{E}_{eff}$ with ratio $\mathcal{E}_{NL}/\mathcal{E}_{eff}(\varepsilon_t) > 1$, *i.e.* greater than one and an increasing function of the linear high-strain range onset ε_t^{NL}. For the generic model-based parameter sets (suffix -M) introduced in Eq. (6) $B = 2.15$ and $k = 2.53$ holds, whereas for the generic approximated parameter sets (suffix -A) given in Eq. (7) $B = 2.21$ and $k = 1.78$. Thus, for the generic parameter sets Eq. (9) local slopes are analytically expressed as

$$\text{for E-M:}\quad \mathcal{E}_{NL}/\mathcal{E}_{eff} = e^{2.15\,\varepsilon_t^{NL}} \qquad (\varepsilon_t^{NL} = 1 \Rightarrow \mathcal{E}_{NL} = 8.58\,\mathcal{E}_{eff}), \tag{9a}$$

$$\text{for C-M:}\quad \mathcal{E}_{NL}/\mathcal{E}_{eff} = 7.59\,(\varepsilon_t^{NL})^2 + 1 \qquad (\varepsilon_t^{NL} = 1 \Rightarrow \mathcal{E}_{NL} = 8.59\,\mathcal{E}_{eff}), \tag{9b}$$

$$\text{for E-A:}\quad \mathcal{E}_{NL}/\mathcal{E}_{eff} = e^{2.21\,\varepsilon_t^{NL}} \qquad (\varepsilon_t^{NL} = 1 \Rightarrow \mathcal{E}_{NL} = 9.12\,\mathcal{E}_{eff}), \tag{9c}$$

$$\text{for C-A:}\quad \mathcal{E}_{NL}/\mathcal{E}_{eff} = 5.34\,(\varepsilon_t^{NL})^2 + 1 \qquad (\varepsilon_t^{NL} = 1 \Rightarrow \mathcal{E}_{NL} = 6.34\,\mathcal{E}_{eff}), \tag{9d}$$

where reference expressions for $\varepsilon_t^{NL} = 1$ are indicated between brackets. For this case ($\varepsilon_t^{NL} = 1$), generic model-based exponential (for E-M) and cubic (for C-M) parameter sets both result in $\mathcal{E}_{NL}/\mathcal{E}_{eff} \approx 8.58$. Ratios obtained for generic approximated parameter sets are either 6% greater (for E-A) or 35% smaller (for C-A) than this reference ratio.

5. Stress–strain parameters and curves: measured and predicted

Experimentally fitted (Section 3.2) and predicted (Section 4) model parameters and resulting stress–strain curves for the three length-based ($\mathrm{II}_{M5,L}$, $\mathrm{III}_{MRI,L}$, $\mathrm{IV}_{EPI,L}$) and three volume-based ($\mathrm{II}_{M5,V}$, $\mathrm{III}_{MRI,V}$, $\mathrm{IV}_{EPI,V}$) silicone composite specimens depicted in Fig. 3 are quantified, compared and discussed.

Table 4
Measured $\mathcal{E}_{eff}$ and modelled $\hat{\mathcal{E}}_{eff}$ (Eq. (5)) low-strain Young's moduli (in kPa).

L-based	$\mathcal{E}_{eff}$ [kPa]	$\hat{\mathcal{E}}_{eff}$ [kPa]	V-based	$\mathcal{E}_{eff}$ [kPa]	$\hat{\mathcal{E}}_{eff}$ [kPa]
$\mathrm{II}_{M5,L}$	8.0	9.5	$\mathrm{II}_{M5,V}$	7.2	6.2
$\mathrm{III}_{MRI,L}$	5.4	3.4	$\mathrm{III}_{MRI,V}$	4.5	3.3
$\mathrm{IV}_{EPI,L}$	5.7	8.5	$\mathrm{IV}_{EPI,V}$	5.0	3.8

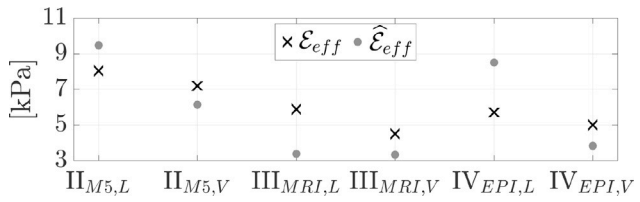

Fig. 6. Low-strain Young's moduli of length-based ($\mathrm{II}_{M5,L}$, $\mathrm{III}_{MRI,L}$ and $\mathrm{IV}_{EPI,L}$) and volume-based ($\mathrm{II}_{M5,V}$, $\mathrm{III}_{MRI,V}$ and $\mathrm{IV}_{EPI,V}$) silicone specimens: measured $\mathcal{E}_{eff}$ (×) and modelled $\hat{\mathcal{E}}_{eff}$ using Eq. (5) (•).

5.1. Low-strain linear elasticity: effective Young's modulus $\mathcal{E}_{eff}$ and $\hat{\mathcal{E}}_{eff}$

Effective low-strain Young's moduli characterising the linear elastic low-strain behaviour are measured as outlined in Section 3.2.1 and modelled using Eq. (5). Measured $\mathcal{E}_{eff}$ and modelled $\hat{\mathcal{E}}_{eff}$ for the three length-based and three volume-based specimens are plotted in Fig. 6. and summarised in Table 4. All effective low-strain Young's moduli, either measured or modelled vary between 3 kPa and 10 kPa. The absolute difference $|\mathcal{E}_{eff} - \hat{\mathcal{E}}_{eff}|$ between measured $\mathcal{E}_{eff}$ and modelled $\hat{\mathcal{E}}_{eff}$ low-strain Young's moduli ranges between 1.0 kPa and 2.8 kPa. Thus, overall values and tendencies observed for modelled $\hat{\mathcal{E}}_{eff}$ agree with those observed for measured $\mathcal{E}_{eff}$ and are within the model accuracy of 3.5 kPa reported previously in Ahmad et al. (2021, 2022).

For modelled $\hat{\mathcal{E}}_{eff}$, the impact ($\mathrm{II}_{M5,.}$, $\mathrm{IV}_{EPI,.}$) or lack thereof ($\mathrm{III}_{MRI,.}$) of the imposed ratio (length-based or volume-based as detailed in Section 2.2) is understood considering the harmonic mean in Eq. (5). The mean depends on individual layer lengths $l_{i=1\ldots n}$ and layer Young's moduli $\mathcal{E}_{i=1\ldots n}$ indicated in Fig. 3. For all specimens, Y_l is larger in the muscle layer than in the superficial layer so that shortening the muscle layer, corresponding to imposing the volume ratio instead of the length ratio, results in reducing $\hat{\mathcal{E}}_{eff}$. The decrease is significant for M5-based (3.4 kPa) and EPI-based (4.7 kPa) replicas. For MRI-based specimens the decrease is not significant (0.1 kPa) as the muscle layer is shortened with less than ≤15% (or ≤5.6 mm) and in addition $\mathcal{E}_i$ of the muscle (4.0 kPa) and superficial (2.2 kPa) layer are of the same order of magnitude.

5.2. Non-linear continuous models: fitted and predicted two-parameter sets

5.2.1. Continuous model accuracy

The exponential (E) and cubic (C) continuous two-parameter relationships (Eq. (4)) with predicted parameter sets, *i.e.* either generic model-based parameter sets (suffix -M, Eq. (6)) or generic approximated parameter sets (suffix -A, Eq. (7)), allow to model the stress–strain behaviour in the range $\varepsilon_t \leq 1.55$. It is reminded that generic two-parameter sets reduce to a one-parameter continuous model as their values depend only on the effective low-strain Young's modulus. Measured $\mathcal{E}_{eff}$ and modelled $\hat{\mathcal{E}}_{eff}$ effective low-strain Young's moduli were given in Table 4.

At first, measured values $\mathcal{E}_{eff}$ are used to determine the generic parameter sets for each specimen in order to consider the accuracy of the generic parameter approach without accounting for errors associated with the modelled effective low-strain Young's modulus $\hat{\mathcal{E}}$. Modelled continuous stress–strain curves are illustrated for the cubic relationship in Fig. 7 for specimens $\mathrm{II}_{M5,L}$, $\mathrm{II}_{M5,V}$, $\mathrm{III}_{MRI,V}$ and $\mathrm{IV}_{EPI,V}$. For comparison, the model outcome with the cubic best fit parameters (C-fit) estimated on the measured stress–strain data is plotted as well. The accuracy of each curve with respect to the measured data is indicated (R^2 in percentage, rmse in kPa) as is low-strain upper limit ε_l. For specimens $\mathrm{III}_{MRI,V}$ and $\mathrm{IV}_{EPI,V}$, the measured strain range yields up to about twice ε_l since $\varepsilon_t \leq 0.49$. Within this range, both C-M and C-A curves provide accurate estimates of the measured data as rmse ≤ 0.39 kPa and $R^2 \geq 95.6\%$. This is in particular the case for the C-M curves for which the associated accuracies approximate the best fit accuracies ($R^2 \geq 99.9\%$ and rmse ≤ 0.03 kPa). For specimens $\mathrm{II}_{M5,L}$ and $\mathrm{II}_{M5,V}$ the measured strain-range is extended, up to about thrice ε_l since $\varepsilon_t \leq 1.08$. The C-A curve ($R^2 = 99.6\%$ and rmse = 0.71 kPa) agrees best with measured data for specimen $\mathrm{II}_{M5,L}$ whereas the C-M curve ($R^2 \geq 99.6\%$ and rmse ≤ 0.89 kPa) provides the best estimate for specimen $\mathrm{II}_{M5,V}$. In general, both the exponential and cubic curves obtained with $\mathcal{E}_{eff}$ and either of the generic parameter sets, *i.e.* model-based (C-M and E-M) or approximated (C-A and E-A), provide a reasonable accuracy as $R^2 > 93\%$ and rmse < 3.6 kPa for all specimens. This shows that when the effective low-strain Young's modulus $\mathcal{E}_{eff}$ is measured, *e.g.* from uni-axial tension tests in the range $\varepsilon_t < 0.25$, the non-linear behaviour for larger strains can be modelled without the need for additional measurements. Thus, the proposed one-parameter model for the continuous stress–strain behaviour is validated for all six replica-based specimens within the measured strain ranges.

In the case that the generic parameter sets for each specimen are determined not from measured $\mathcal{E}_{eff}$, but from modelled $\hat{\mathcal{E}}_{eff}$, the continuous stress–strain behaviour is estimated solely from the composition of each composite specimen (Eq. (5)) without any measurement on the composite specimen. As modelled $\hat{\mathcal{E}}_{eff}$ provide a close, but not exact match to $\mathcal{E}_{eff}$ (Table 4) the accuracy found for the exponential and cubic curves for generic parameter sets based on $\hat{\mathcal{E}}_{eff}$ is expected to reduce. Nevertheless, as for all specimens $R^2 > 79\%$ and rmse < 5.0 kPa hold, generic parameter sets based on $\hat{\mathcal{E}}_{eff}$ still provide an acceptable accuracy. This is of particular interest aiming for the structural design of specimens as the approach allows to reasonably predict the overall stress–strain behaviour without any measurement.

5.2.2. Curves with generic two-parameters sets: strain-range up to 1.55

Generic two-parameters sets are derived for strains up to 1.55 at most. Beyond this strain limit, the assumption of the nearly matching exponential and cubic relationships fails (Ahmad et al., 2023). This full strain range ($\varepsilon_t < 1.55$) is used to compare the stress–strain behaviour of all six specimens for the cubic relationship. Curves obtained using generic model-based parameter set (C-M) with measured $\mathcal{E}_{eff}$ (Table 4) for the length-based and volume-based specimens are plotted in Fig. 8. As expected, curves for specimens with similar low-strain Young's modulus $\mathcal{E}_{eff}$ are in close agreement. This is the case for specimens $\mathrm{IV}_{EPI,L}$ and $\mathrm{III}_{MRI,L}$ ($\mathcal{E}_{eff}$-difference of 0.3 kPa or 5%) and for specimens $\mathrm{IV}_{EPI,V}$ and $\mathrm{III}_{MRI,V}$ ($\mathcal{E}_{eff}$-difference of 0.5 kPa or 10%). The stress–strain curves increase more rapidly with $\mathcal{E}_{eff}$, as values of the generic two-parameter sets increase, so that curves for M5-based specimens ($\mathrm{II}_{M5,L}$ and $\mathrm{II}_{M5,V}$) are increased compared to curves for MRI-based ($\mathrm{III}_{MRI,L}$ and $\mathrm{III}_{MRI,V}$) and EPI-based ($\mathrm{IV}_{EPI,L}$ and $\mathrm{IV}_{EPI,V}$) specimens. For the same reason, stresses associated with length-based specimens are increased compared to volume-based specimens. Thus, this illustrates that the continuous relationships with generic two-parameter sets become de-facto a one-parameter model approach, so that the modelled non-linear stress–strain behaviour can be explained in terms of their low-strain elastic Young's modulus.

5.2.3. Linear low-strain elasticity

The low-strain Young's modulus is related to the parameters of the exponential and cubic relationships as $A\,B$ and b, respectively (Section 4.2). For generic parameter sets, obtained from the low-strain Young's modulus, ratios $A\,B/\mathcal{E}_{eff}$ and $b/\mathcal{E}_{eff}$ are constant:

$$\text{generic model-based - constant ratio: } \frac{A\,B}{\mathcal{E}_{eff}} = 1, \quad \frac{b}{\mathcal{E}_{eff}} = 1, \quad (10a)$$

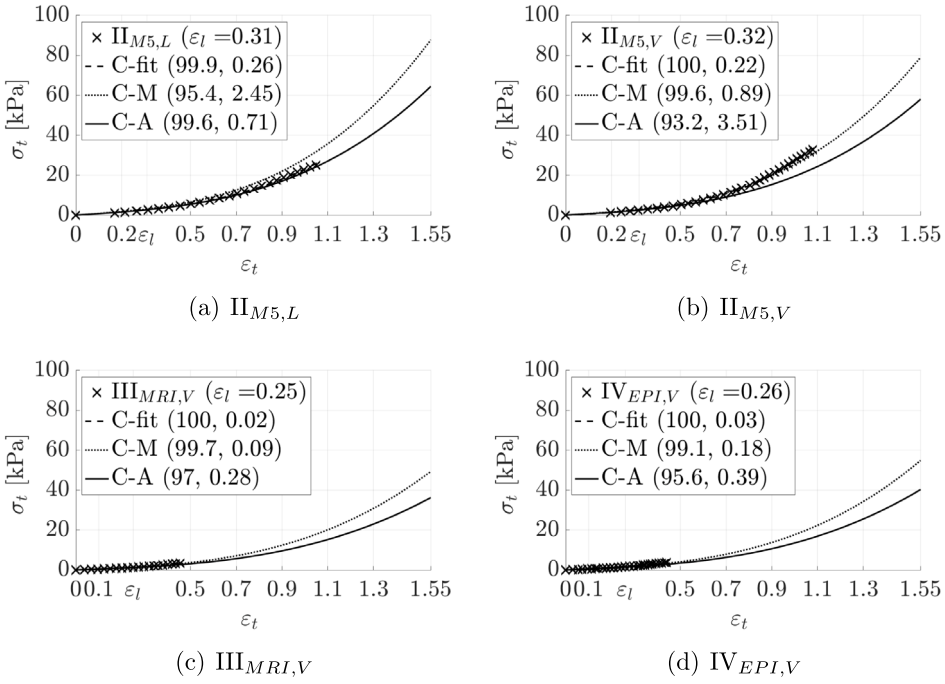

Fig. 7. Illustration of measured (×) stress–strain data $\sigma_t(\varepsilon_t)$ and their cubic best fit (C-fit): (a) II$_{M5,L}$, (b) II$_{M5,V}$, (c) III$_{MRI,V}$ and d) IV$_{EPI,V}$. Modelled cubic curves ($\varepsilon_t \leq 1.55$) with generic model-based parameter sets (C-M) and generic approximated parameter sets (C-A) obtained using measured $\mathcal{E}_{eff}$. Cubic curve accuracies (R^2 in %, rmse in kPa) and low-strain upper limit ε_l are indicated.

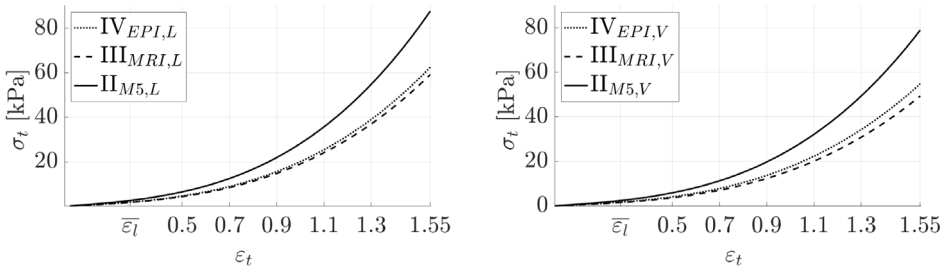

Fig. 8. Cubic stress–strain curves $\sigma_t(\varepsilon_t)$ for generic model-based parameter sets (C-M) with measured $\mathcal{E}_{eff}$: (a) length-based specimens (IV$_{EPI,L}$, III$_{MRI,L}$, II$_{M5,L}$), (b) volume-based specimens (IV$_{EPI,V}$, III$_{MRI,V}$, II$_{M5,V}$). Mean low-strain upper limit $\overline{\varepsilon_l} = 0.28$ is indicated.

generic approximated - constant ratio: $\dfrac{\hat{A}\,\hat{B}}{\mathcal{E}_{eff}} = 0.73, \quad \dfrac{\hat{b}}{\mathcal{E}_{eff}} = 0.92.$ (10b)

Ratios associated with best fit parameter estimates obtained by fitting the exponential (E-fit, $(\hat{A}, \hat{B})$) and cubic (C-fit, $(\hat{a}, \hat{b})$) relationships to the measured stress–strain data are plotted in Fig. 9. Plotted values vary between 0.6 and 0.92 and thus less than unity, *i.e.* the constant for the generic model-based parameters (Eq. (10a)). Mean values (lines) are indicated and yield:

best fit - mean ratio: $\overline{\hat{A}\hat{B}/\mathcal{E}}_{eff} = 0.67, \quad \overline{\hat{b}/\mathcal{E}}_{eff} = 0.77.$ (11a)

Standard deviations are small, 9% (±0.06 for $\hat{A}\,\hat{B}/\mathcal{E}_{eff}$) and 12% (±0.09 for $\hat{b}/\mathcal{E}_{eff}$), and mean values are of the same magnitude as the constants of the generic approximated parameter sets (Eq. (10b). Thus ratios estimated on the data approximate the constant values associated with the generic parameter sets. Thus, overall fitted ratios confirm that continuous relationships for generic parameters allow to capture the low-strain stress behaviour for the replica-based specimens.

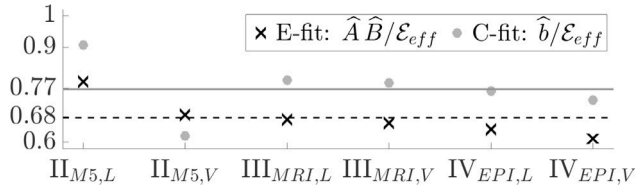

Fig. 9. Ratios $\hat{A}\,\hat{B}/\mathcal{E}_{eff}$ (×) and $\hat{b}/\mathcal{E}_{eff}$ (•) between best fit parameters, obtained from fitting the exponential (E-fit) and cubic (C-fit) relationships to the measured stress–strain data, and the measured low-strain Young's modulus $\mathcal{E}_{eff}$ for length-based (II$_{M5,L}$, III$_{MRI,L}$ and IV$_{EPI,L}$) and volume-based (II$_{M5,V}$, III$_{MRI,V}$ and IV$_{EPI,V}$) silicone specimens. Mean values for $\hat{A}\,\hat{B}/\mathcal{E}_{eff}$ (dashed line) and $\hat{b}/\mathcal{E}_{eff}$ (full line) are indicated as well.

5.2.4. Linear high-strain elasticity: effective Young's modulus and onset

The linear high-strain range is fully characterised by its effective high-strain Young's modulus $\mathcal{E}_{NL}$ and onset strain ε_t^{NL}. Concretely, $\mathcal{E}_{NL}$ is obtained as the slope of a linear fit to interval $[\varepsilon_t^{NL}\ 1.55]$ on the curves obtained from the continuous exponential and cubic relationships with generic parameter sets (E-M, E-A, C-M and C-A). The influence of onset strain ε_t^{NL} on the estimated slope and the linear fit

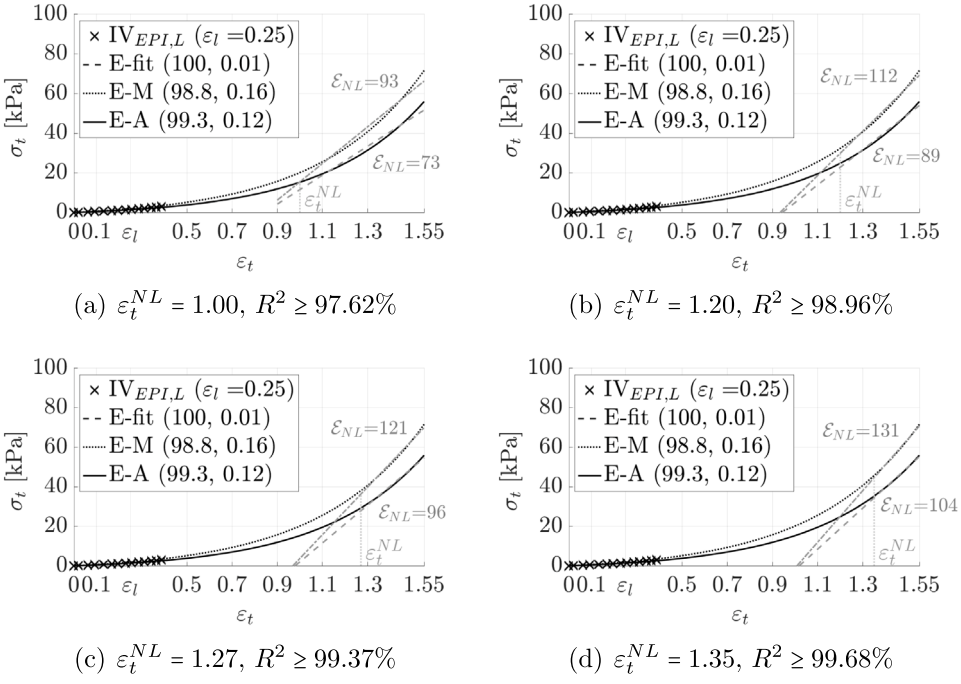

Fig. 10. Influence of high strain onset $\varepsilon_t^{NL} \in \{1.00, 1.20, 1.27, 1.35\}$ (subplots) on slope $\mathcal{E}_{NL}$ (in kPa) and accuracy (min(R^2) in %) of linear fits (grey lines) to intervals $[\varepsilon_t^{NL}\ 1.55]$ for exponential stress–strain curves $\sigma_t(\varepsilon_t)$ obtained with generic model-based (E-M) and with generic approximated (E-A) parameter sets for specimen IV$_{EPI,L}$ ($\mathcal{E}_{eff}$ = 5.7 kPa). Measured (×) stress–strain data and their exponential best fit (E-fit) are plotted as well. Model and fit accuracies (R^2 in %, rmse in kPa) and low-strain limit ε_l are given.

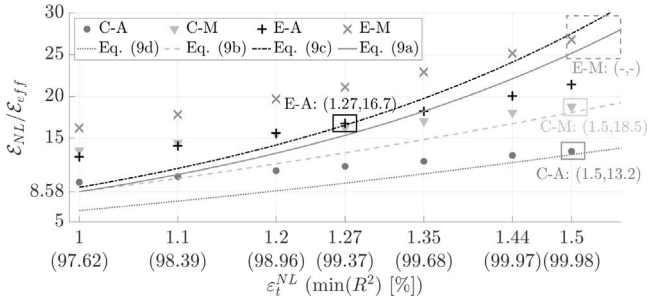

Fig. 11. Ratio (symbols) of the high-strain to low-strain effective Young's modulus $\mathcal{E}_{NL}/\mathcal{E}_{eff}(\varepsilon_t^{NL})$ with $\mathcal{E}_{NL}$ obtained as the slope of linear fits (min(R^2) in %) to intervals $[\varepsilon_t^{NL}\ 1.55]$ for $\varepsilon_t^{NL} \in \{1, 1.1, 1.2, 1.27, 1.35, 1.44, 1.5\}$ on exponential and cubic curves with generic model-based or generic approximated parameter sets: C-A (•), C-M (▾), E-A (+) and E-M (×). Ratios obtained analytically from local slope expressions (Eq. (9)) are plotted (lines) as well. Values $(\varepsilon_t^{NL}, \mathcal{E}_{NL}/\mathcal{E}_{eff})$ (rectangular frames) at which local and linear slopes match (up to the first decimal place leading to first decimal criterion FDC) are indicated. Plotted ratios are specimen independent.

accuracy (R^2) is illustrated in Fig. 10 for specimen IV$_{EPI,L}$. Linear fits to the interval $[\varepsilon_t^{NL}\ 1.55]$ of exponential curves with generic model-based (E-M) and generic approximated (E-A) parameter sets are plotted for four different onset strains, $\varepsilon_t^{NL} \in \{1.00, 1.20, 1.27, 1.35\}$. The high-strain linear slope $\mathcal{E}_{NL}$ is indicated for each generic parameter set and the minimum linear fit accuracy R^2 for both parameter sets is indicated. It is seen that regardless of ε_t^{NL}, slopes $\mathcal{E}_{NL}$ obtained using generic model-based (E-M) parameter sets are 26% greater than those found for generic approximated (E-A) parameter sets. Fig. 10 illustrates that $\mathcal{E}_{NL}$ (with 30%) and R^2 (from 97.62% to 99.68%) increase with ε_t^{NL}, *i.e.* when the fit interval is shortened.

A systematic overview of effective high-strain Young's modulus $\mathcal{E}_{NL}$ normalised with effective low-strain Young's modulus $\mathcal{E}_{eff}$ as a function ε_t^{NL} is provided in Fig. 11. Slopes estimated from linear fits (symbols) to intervals $[\varepsilon_t^{NL}\ 1.55]$ on exponential and cubic curves with generic model-based and with generic approximated parameter sets (C-A, C-M, E-A and E-M), as illustrated in Fig. 10, are obtained for seven ε_t^{NL}-values between 1 and 1.5. For each ε_t^{NL}, the overall minimum linear fit accuracy, which corresponds to values obtained for exponential curves, is indicated between brackets. The minimum fit accuracy $R^2 \geq 97.62\%$ (or $R^2 \geq 98.97\%$ for cubic curves) is sufficiently large to argue that linear fits provide a good approximation of modelled non-linear stress–strain curves in the intervals $[\varepsilon_t^{NL}\ 1.55]$ with $\varepsilon_t^{NL} \geq 1$. Nevertheless, in order to potentially extend the linear range continuously beyond the range $\varepsilon_t = 1.55$, a fit accuracy of $R^2 \leq 99\%$ seems necessary, *e.g.* when comparing the overlap of modelled continuous curves and high-strain linear fits for $\varepsilon_t^{NL} = 1$ ($R^2 \geq 97.62\%$) and $\varepsilon_t^{NL} = 1.27$ ($R^2 \geq 99.37\%$) in Fig. 10. It is noted that plotted ratios $\mathcal{E}_{NL}/\mathcal{E}_{eff}$ obtained on curves with generic parameter sets are specimen independent due to the normalisation by $\mathcal{E}_{eff}$.

Ratios of linear slopes $\mathcal{E}_{NL}/\mathcal{E}_{eff}$ are further compared to values resulting from the analytical local slope expressions summarised in Eq. (9). Normalised local slopes are plotted (lines) as function of ε_t^{NL} in Fig. 11 for C-A using Eq. (9d), for C-M using Eq. (9b), for E-A using Eq. (9c) and for E-M using Eq. (9a). Values $(\varepsilon_t^{NL}, \mathcal{E}_{NL}/\mathcal{E}_{eff})$ at which linear and local slopes match up to the first decimal place (first decimal criterion, FDC) are indicated in Fig. 11 and summarised in Table 5. It is noted that this criterion indeed ensures that linear fits are a continuous extension of the non-linear curves, either exponential or cubic. From Table 5 follows that the exponential relationship with generic approximated parameter set (E-A) is associated with the largest, and hence most meaningful, high-strain interval $[\varepsilon_t^{NL}\ 1.55]$ with $\varepsilon_t^{NL} = 1.27$. In addition, associated ratios $\mathcal{E}_{NL}/\mathcal{E}_{eff}$ are in between values found for the cubic relationship with generic model parameters (C-M and C-A). Moreover, the E-A model results in the best overall model accuracy ($R^2 = 98 \pm 3\%$) (Ahmad et al., 2023). Therefore, the E-A model approach ($\mathcal{E}_{NL} \approx 16.7\,\mathcal{E}_{eff}$) is used to estimate high-strain Young's moduli $\mathcal{E}_{NL}$ for all specimens. Resulting $\mathcal{E}_{NL}$ are summarised in Table 6.

Thus, the potential of a high-strain extension leads to favour the non-linear exponential relationship (E-A) with generic exponential approximated parameters $A = \mathcal{E}_{eff}/3.03$ and $B = 2.21$. When accounting

Table 5
Overview of high strain onset ε_t^{NL} and normalised high-strain Young's modulus $\mathcal{E}_{NL}/\mathcal{E}_{eff}$ indicated in Fig. 11 obtained with the first decimal criterion (FDC).

FDC applied to	ε_t^{NL}	$\mathcal{E}_{NL}/\mathcal{E}_{eff}$
C-A and Eq. (9d)	1.5	13.2
C-M and Eq. (9b)	1.5	18.5
E-A and Eq. (9c)	1.27	16.7
E-M and Eq. (9a)	–	–

Table 6
High-strain Young's moduli $\mathcal{E}_{NL} \approx 16.7\,\mathcal{E}_{eff}$.

L-based	$\mathcal{E}_{NL}$ [kPa]	V-based	$\mathcal{E}_{NL}$ [kPa]
$\mathrm{II}_{M5,L}$	134	$\mathrm{II}_{M5,V}$	120
$\mathrm{III}_{MRI,L}$	90	$\mathrm{III}_{MRI,V}$	75
$\mathrm{IV}_{EPI,L}$	95	$\mathrm{IV}_{EPI,V}$	84

for a linear high-strain range for $\varepsilon_t \geq \varepsilon_t^{NL}$, the stress–strain relationship for the replica-based specimens becomes:

$$\begin{aligned}\sigma_t(\varepsilon_t) &= A\,(e^{B\,\varepsilon_t} - 1) && \text{for } \varepsilon_t \leq \varepsilon_t^{NL},\\ &= \mathcal{E}_{NL}\,\varepsilon_t + A\,(e^{B\,\varepsilon_t^{NL}} - 1) && \text{for } \varepsilon_t > \varepsilon_t^{NL},\end{aligned} \tag{12}$$

with strain onset $\varepsilon_t^{NL} = 1.27$ and effective high-strain Young's modulus $\mathcal{E}_{NL} = 16.7\,\mathcal{E}_{eff}$. It is noted, that Eq. (12) remains a one-parameter approach as the stress–strain behaviour can be determined from the effective low-strain Young's modulus $\mathcal{E}_{eff}$. Eq. (12) allows to extent the one-parameter approach for the replica-based specimens to the linear high-strain range and thus to remove the strain limit (up to 1.55).

6. Conclusion

Uni-axial tension test data on six composite specimens derived from three multi-layer silicone vocal folds replicas allowed to validate a one-parameter continuous non-linear model approach for silicone composites, which allows to explain the stress–strain behaviour from the effective low-strain Young's modulus of each homogenised specimen. The effective low-strain Young's modulus (between 3 and 10 kPa) is either measured as the slope of linear low-strain range (up to ≈0.28) or modelled (accuracy between 1 and 2.8 kPa) from the specimens layer composition. Although that the stress–strain model accuracy is greater for measured ($R^2 > 93\%$, rmse < 3.6 kPa) than for modelled ($R^2 > 79\%$, rmse < 5 kPa) values of the low-strain Young's modulus, it is shown that in both cases the stress–strain behaviour can be explained as a function of the composite structure by means of the effective low-strain Young's modulus. This implies that the one-parameter model approach is validated in the low-strain and non-linear strain region. To potentially extend the model approach beyond the strain limit of 1.55, a criterion is proposed to identify a linear high-strain region with onset 1.27 and with effective high-strain Young's modulus equal to 16.7 times the effective low-strain Young's modulus. This linear high-strain range provides a continuous extension to the exponential relationship with generic approximated parameter set for strains smaller than the high-stain onset 1.27. Overall, it is shown that a one-parameter model approach allows to model and explain the non-linear stress–strain relationship from its effective low-strain Young's modulus and thus to provide a quantitative stress–strain behaviour comparison of composites used to mold vocal fold replicas. In addition, the influence of the structural design of silicone composites for vocal fold replicas with structural changes, either normal or abnormal, on the stress–strain behaviour can be systematically assessed without any measurement or with uni-axial testing solely within the low-strain limit (between 0.25 and 0.32). As so far, no measure-free analytical model approach was available, the assessed approach is expected to encourage further research.

Declaration of competing interest

The authors declare the following financial interests/personal relationships which may be considered as potential competing interests: Annemie Van Hirtum reports financial support was provided by French National Research Agency (ANR-20-CE23-0008-23). Mohammad Ahmad reports financial support was provided by French Government Ministry of National Education.

Data availability

Data will be made available on request.

Acknowledgements

This work was partly supported by Full3DTalkingHead project (ANR-20-CE23-0008-03) and a Ph.D. grant (French Ministry of Education and Research).

References

Ahmad, M., Bouvet, A., Pelorson, X., Van Hirtum, A., 2021. Modelling and validation of the elasticity parameters of multi-layer specimens pertinent to silicone vocal fold replicas. Int. J. Mech. Sci. 208, 106685.
Ahmad, M., Pelorson, X., Fernández, A., Guasch, O., Van Hirtum, A., 2022. Low-strain effective Young's modulus model and validation for multi-layer vocal fold-based silicone specimens with inclusions. J. Appl. Phys. 131, 054701.
Ahmad, M., Pelorson, X., Guasch, O., Fernández, A., Van Hirtum, A., 2023. Modelling and validation of the non-linear elastic stress–strain behaviour of multi-layer silicone composites. J. Mech. Behav. Biomed. Mater. 139, 105690.
Alexander, N., Wang, K.Y., Jiang, K., Ongkasuwan, J., Lincoln, C., 2021. Volumetric analysis of the vocal folds using computed tomography: effects of age, height, and gender. Laryngoscope 131, E240–E247.
Alipour, F., Titze, I., 1991. Elastic models of vocal fold tissues. J. Acoust. Soc. Am. 90, 1326–1331.
Berke, G., Gerratt, B., 1993. Laryngeal biomechanics: an overview of mucosal wave mechanics. J. Voice 7, 123–128.
Bouvet, A., 2019. Experimental and Theoretical Contribution to the Analysis and the Modelling of the Vocal Folds Vibration. (Ph.D. thesis). Grenoble Alpes University, France.
Bouvet, A., Tokuda, I., Pelorson, X., Van Hirtum, A., 2020b. Influence of level difference due to vocal folds angular asymmetry on auto-oscillating replicas. J. Acoust. Soc. 147, 1136–1145.
Bouvet, A., Tokuda, I., Pelorson, X., Van Hirtum, A., 2021. Imaging of auto-oscillating vocal folds replicas with left–right level difference due to angular asymmetry. Biomed. Signal Process. Control 63, 1–12.
Chan, R., Fu, M., Young, L., Tirunagari, N., 2007. Relative contributions of collagen and elastin to elasticity of the vocal fold under tension. Ann. Biomed. Eng. 35, 1471–1483.
Chhetri, D., Zhang, Z., Neubauer, J., 2011. Measurement of Young's modulus of vocal folds by indentation. J. Voice 25, 1–7.
Fung, Y., 1967. Elasticity of soft tissues in simple elongation. Am. J. Physiol. 213, 1605–1624.
Fung, Y., 2010. Biomechanics. Springer.
Hirano, M., Kurita, S., Nakashima, T., 1983. Vocal Fold Physiology: Contempory Research and Clinical Issues. College-Hill Press, pp. 22–43.
Min, Y., Titze, I., Alipour, F., 1995. Stress–strain response of the human vocal ligament. Ann. Otol. Rhinol. Laryngol. 104, 563–569.
Miri, A., 2014. Mechanical characterization of vocal fold tissue: a review study. J. Voice 28, 657–666.
Mobashir, M., Mohamed, A., Quriba, A., Anany, A., Hassan, E., 2018. Linear measurements of vocal folds and laryngeal dimensions in freshly excised human larynges. J. Voice 32, 525–529.
Murray, P., Thomson, S., 2012. Vibratory responses of synthetic, self-oscillating vocal fold models. J. Acoust. Soc. Am. 132, 3428–3438.
O'Shaughnessy, D., 1987. Speech Communication Human and Machine. Addison-Wesley Publishing Company.
Pickup, B., Thomson, S., 2010. Flow-induced vibratory response of idealized versus magnetic resonance imaging-based synthetic vocal fold models. J. Acoust. Soc. Am. 128, 124–129.
Plant, R., Freed, G., Plant, R., 2004. Direct measurement of onset and offset phonation threshold pressure in normal subjects. J. Acoust. Soc. Am. 116, 3640–3646.
Reuss, A., 1929. Berechnung der fließgrenze von mischkristallen auf grund der plastizitätsbedingung für einkristalle. ZAMM Z. Angew. Math. Mech. 9, 49–58.

Riede, T., Brown, C., 2013. Body size, vocal fold length, and fundamental frequency: implications for mammal vocal communication. Nova Acta Leopoldina NF 111 (380), 295–314.

Rosen, C., Simpson, C., 2008. Operative Techniques in Laryngology. Springer-Verlag.

Scherer, R., Shinwari, D., De Witt, K., Zhang, C., Kucinschi, B., Afjeh, A., 2001. Intraglottal pressure profiles for a symmetric and oblique glottis with a divergence angle of 10 degrees. J. Acoust. Soc. Am. 109, 1616–1630.

Tanaka, M., Weisenbach, C., Miller, M., Kuxhaus, L., 2011. A continuous method to compute model parameters for soft biological materials. J. Biomed. Eng. 133, 1–7.

Titze, I., 2011. Vocal fold mass is not a useful quantify for describing f_0 in vocalization. J. Speech Lang. Hear. Res. 54, 520–522.

Tokuda, I., Shimamura, R., 2017. Effect of level difference between left and right vocal folds on phonation: Physical experiment and theoretical study. J. Acoust. Soc. Am. 142, 482–492.

Van Hirtum, A., Bouvet, A., Tokuda, I., Pelorson, X., 2022. Dynamic vibration mode decomposition of auto-oscillating vocal fold replicas without and with vertical tilting. J. Sound Vib. 516, 116504.

Zhang, Z., Samajder, H., Long, J., 2017. Biaxial mechanical properties of human vocal fold cover under fold elongation. J. Acoust. Soc. Am. 29, EL356.